THE JOURNAL OF PHYSICAL CHEMISTRY C
A JOURNAL OF THE AMERICAN CHEMICAL SOCIETY

Laser-Induced Sulfur Vacancy Defect Healing by Oxygen in Molybdenum Disulfide Monolayers

Ermes Peci,* Yang Pan, Emma Spotorno, Lorenzo Ramò, Francesca Telesio, Michele Magnozzi, Zygmunt Miłosz, Luca Gregoratti, Matteo Amati, Nicolò Petrini, Ilka Kriegel, Dietrich R. T. Zahn, Maurizio Canepa, and Francesco Bisio

Cite This: *J. Phys. Chem. C* 2025, 129, 21407−21417

Read Online

ACCESS | Metrics & More | Article Recommendations | Supporting Information

ABSTRACT: The photoluminescence yield of monolayer MoS_2 was locally and durably enhanced by prolonged laser exposure, with significant alterations of the spectral weight of its exciton and trion subcomponents. Evidence from Raman and photoluminescence spectroscopy, tip-enhanced photoluminescence, atomic force microscopy, and photoemission spectroscopy allows the phenomenon to be rationalized as a photoinduced oxidation of sulfur vacancies mediated by ambient air. A decrease in the trion emission and a marked blue shift of the A_1' Raman peak suggest p-type counterdoping. Nanoscale spectroscopies reveal that the enhanced photoluminescence emission comes from the very edge of the patterning laser spot, where photoinduced oxidation has occurred.

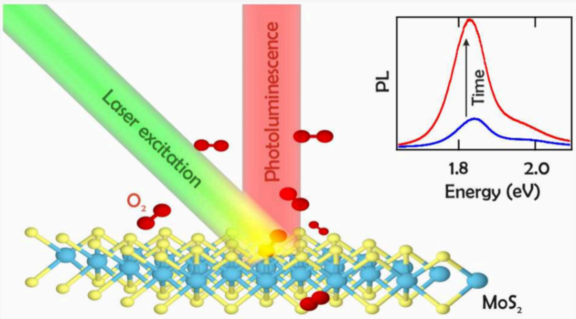

■ INTRODUCTION

Two-dimensional (2D) transition metal dichalcogenides (TMDCs) are a class of layered materials renowned for their remarkable optical and electronic properties, making them some of the most studied materials of the past decade.[1,2] Semiconducting TMDCs, such as MoS_2 and WS_2, exhibit an indirect-to-direct bandgap transition when thinned down to a monolayer, leading to a strong photoluminescence (PL) response in the visible range.[3,4] Moreover, strong excitonic effects,[5,6] bandgap tunability,[7,8] spin-valley coupling,[9,10] and symmetry-dependent effects[11,12] make semiconducting TMDCs a fascinating playground for fundamental research and next-generation electronic and photonic devices.[13−16]

Defects such as vacancies, dislocations, impurities, and grain boundaries play a major role in tailoring the optical properties of any TMDC crystal.[17] Defects may hamper the optical performances of TMDC-based devices; in particular, chalcogenide vacancies mediate the nonradiative recombination of the excitons, hence lowering the PL quantum yield (PLQY),[18−20] which is a key figure of merit for optoelectronic devices.[21,22] Natural MoS_2 can exhibit a surface defect density up to 8% of the surface area,[23] meaning that the tailoring of the optoelectronic response of these materials almost necessarily involves the engineering of such chemical or crystalline nonidealities.[24,25]

Many different strategies have been developed to enhance the PLQY of TMDC monolayers. Thermal annealing was reported to improve the PLQY of monolayer MoS_2 (1L MoS_2)[26] by means of oxygen adsorption at S vacancies (V_S), leading to p-doping and consequently switching from trion-dominated to exciton-dominated emission.[27,28] Even more pronounced enhancements can be achieved with chemical treatments, which often rely on the nonoxidizing superacid bis(trifluoromethane)sulfonimide (TFSI).[21,22,29−33] However, the harsh chemical behavior of superacids limits the range of applications of this kind of treatments.[21,34] The TFSI treatment is believed to induce an electron counter-doping (hole doping), thereby suppressing the nonradiative trion recombination in favor of the radiative exciton emission.[35] Hole doping capability is also achieved with other chemical treatments with similar effects on the PLQY, e.g., 7,7,8,8-tetracyanoquinodimethane (TCNQ)[36] or hydrohalic acids.[37] Another treatment involves poly(4-styrenesulfonate) (PSS), which was proposed for a V_S "self-healing" mechanism, in which the hydrogenation of PSS guides sulfur adatom clusters on the MoS_2 surface to heal V_S.[34] Notably, oxygen plasma treatments were reported to quench the PL emission in MoS_2.[33] Similarly, the growth of aluminum or hafnium oxides results in a significant reduction of the PL emission, together with a broadening of the PL spectral features.[32,38,39] It is worth noting that the PL line shape and the trion emission can be manipulated in several ways. Strain is known to promote the conversion of exciton into trions[40] and increase their binding energy.[41] Similarly, gating,[42] substrate-induced doping,[43] chemical treatments,[44] and the orbital angular

Received: August 11, 2025
Revised: October 29, 2025
Accepted: November 4, 2025
Published: November 20, 2025

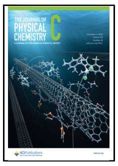

https://doi.org/10.1021/acs.jpcc.5c05608
J. Phys. Chem. C 2025, 129, 21407−21417

momentum of the incident light[45] heavily affect the PL line shape and the exciton/trion ratio.

An alternative to the aforementioned chemical treatments is laser exposure, which was reported to increase the PLQY of monolayer TMDCs to variable extents.[46−50] Laser exposure is a versatile method, which can be applied to any kind of sample; it also allows a selective enhancement on specific micron-sized areas; indeed, it was proposed as a microsteganography technique.[51] However, an in-depth and systematic investigation of the dynamics and physiochemical modifications underlying the laser-induced PL enhancement is still lacking.

Here, we present a comprehensive investigation of the laser-induced PL enhancement mechanism on 1L of MoS_2. We show that a careful tuning of the experimental parameters can lead to a PL enhancement up to 1 order of magnitude with respect to the pristine sample. This enhancement is accompanied by a sharp shift from trion to exciton emission, the suppression of the B exciton contribution, and a blue shift of all the PL peaks. Tip-enhanced photoluminescence spectroscopy (TEPL) and atomic force microscopy (AFM) demonstrate that the enhanced PL emission does not come from the entire circular area corresponding to the laser spot, but from the very edge of a micrometric hole created on the TMDC monolayer by the laser beam. Chemical mapping, performed by means of X-ray photoelectron spectroscopy (XPS) with submicrometric resolution at the ESCA Microscopy beamline at the Elettra synchrotron light source,[52] allows linking this enhancement with laser-induced oxidation of the V_S at the edge of the hole. Finally, intermittent laser irradiation allows understanding the time evolution of the PL enhancement phenomenon in terms of a photoinduced process, triggered after the formation of a pit in the TMDC monolayer and ruling out thermal oxidation at a specific threshold temperature.

EXPERIMENTAL METHODS

Large-Area MoS_2 Exfoliation. Large-area 1L MoS_2 flakes were exfoliated from a bulk synthetic crystal (HQ Graphene, Netherlands) on APTES-functionalized SiO_2 (285 nm)/Si substrates, adopting the exfoliation recipe reported in our previous work.[53] In our method, a thermal release tape (TRT) is used to peel off a 150 nm thick Au layer from a Si substrate; immediately afterward, the Au/TRT stack, exposing a fresh, hydrophilic gold surface,[54] is gently pressed onto a freshly cleaved bulk MoS_2 crystal and subsequently pressed on the APTES-functionalized silicon substrate. The TRT is detached by heating the system above the TRT release temperature, and the gold film is etched away, leaving a large-area crystal on the functionalized substrate. The APTES functionalization is critical for the process to be successful: indeed, without this step, the gold film would detach from the substrate due to the strain induced during the heating stage of the TRT, preventing the successful transfer of the 1L MoS_2 from the gold film to the Si substrate. We deposit APTES on our substrates with 30 cycles of atomic layer deposition (ALD); alternatively, equivalent results were achieved by immersing the substrates in a 0.5% (v/v) APTES/ethanol solution for 20 min and subsequently rinsing them with clean ethanol.

Imaging Spectroscopic Ellipsometry. Imaging spectroscopic ellipsometry (iSE) mapping was performed with a Park Systems Accurion EP4 imaging ellipsometer equipped with a laser-stabilized xenon lamp and a grating monochromator. iSE mapping was performed while operating the instrument as a rotating compensator ellipsometer; hyperspectral maps were acquired at 129 selected wavelengths in the 360−1000 nm range with a 50° angle of incidence. A relatively small angle of incidence was chosen to optimize the signal-to-noise ratio. The focus of the 5× objective was scanned over the probed area, thus achieving a fully focused iSE map while operating the optical system at oblique incidence.

Laser Irradiation, Raman and Photoluminescence Spectroscopies. A Horiba XploRA Plus Raman spectrometer, equipped with a DPSS 532 nm laser, was adopted for the laser irradiation of 1L MoS_2. The excitation power of 10 mW was focused to a spot with a diameter of about ~2 μm using a 50×, 0.5 NA objective, yielding ~0.6 MW/cm^2 power density. Raman and PL hyperspectral mapping were performed with the same instrument, equipped with a motorized sample stage. For Raman mapping, the 532 nm laser was focused by a 100×, 0.9 NA objective, with a nominal power of 0.1 mW delivered to the sample. Raman scattered light was dispersed using a 2400 grooves/mm grating and detected by a Peltier-cooled EMCCD. To achieve a good lateral resolution, Raman mapping was performed with a 0.3 μm step size. Raman spectra were corrected for spectral shifts by using the Si peak from the underlying substrate at 520.7 cm^{-1}.

Laser patterning of the 5 × 5 array used for XPS measurements was performed by using a Jasco NRS-4100 Raman spectrometer, equipped with a DPSS 532 nm laser. A laser intensity of 25 mW was focused to a spot with a diameter of about 3 μm using a 20×, 0.4 NA objective, yielding a ~0.7 MW/cm^2 intensity. Subsequent PL mapping (Figure 6d) was performed using a 100×, 0.9 NA objective, with 0.25 mW excitation power at 532 nm, and the resulting PL signal was dispersed onto a Peltier-cooled CCD by a 900 grooves/mm grating.

Tip-Enhanced Photoluminescence Spectroscopy and Atomic Force Microscopy. TEPL measurements were performed with a Horiba XploRA Plus Raman spectrometer combined with the AIST-NT SmartSPM 1000 atomic force microscope. A 532 nm laser was focused by a 100×, 0.7 NA objective onto a silver-coated tip in a side-illumination geometry, with a 65° incidence from the sample normal. The experimental protocol involves the acquisition of PL spectra with the tip in contact with the sample, corresponding to the sum of the near-field and the far-field signals, and with the tip lifted, corresponding to the far-field signal only. The TEPL analysis is then carried out on the spectra resulting from the far-field subtraction,[55,56] thereby isolating the tip-enhanced contribution. All data shown are background-subtracted. TEPL was performed in nongap mode due to the insulating nature of the SiO_2 substrates. The magnitude of tip-enhancement was not sufficient for TERS. The AIST-NT SmartSPM 1000 setup employed for TEPL measurements was also used as a standalone instrument for AFM measurements, performed using a regular tapping-mode AFM tip.

X-ray Photoelectron Spectroscopy. High-resolution XPS spectra and photoelectron microscopy maps were acquired at the ESCA Microscopy beamline of the Elettra Synchrotron Light Source.[52,57] The experimental setup allowed both the acquisition of high-resolution XPS spectra on a selected area, the size of which can be varied through the beam focusing system, and the acquisition of chemical maps, in which the spectroscopic capability is achieved through a 48-channel detector while raster-scanning the sample.[57] Therefore, elemental mapping comes with spectral analysis within the few-eV energy range of the detector. During the acquisition of high-resolution XPS

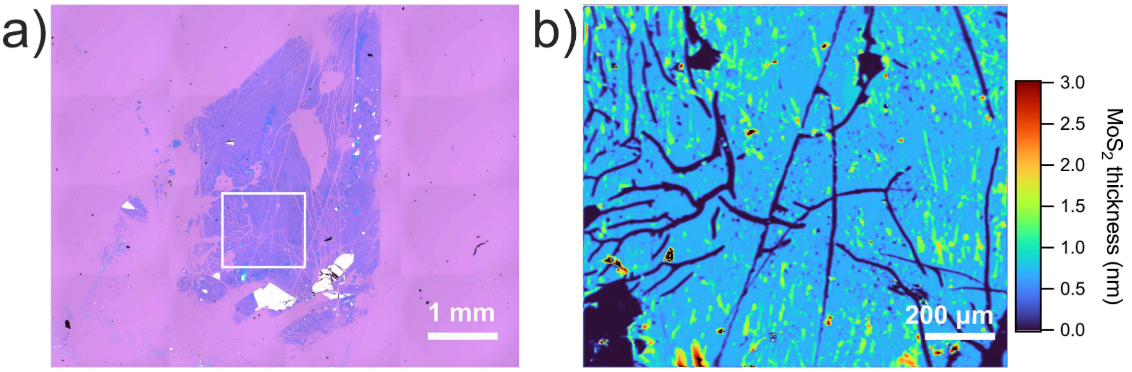

Figure 1. a) Optical microscopy image of a large-area exfoliated 1L MoS_2 crystal onto a SiO_2 (285 nm) substrate. b) Thickness mapping obtained by means of iSE, corresponding to the area marked with the white rectangle in (a). Most of the area exhibits a fitted thickness of 0.7 nm, corresponding to 1L MoS_2, with few small bilayer areas.

spectra, the X-ray spot was intentionally defocused to a diameter of 9 μm to mitigate sample damage from the X-ray beam by decreasing its brilliance. During the subsequent chemical mapping, the X-ray beam was focused by a zone plate and an order sorting aperture down to a diameter of 150 nm, thereby resolving the fine structure of the pattern. Further details are provided in section SI6. All measurements were performed with an incident photon energy of 688.9 eV. Binding energy correction of the high-resolution XPS spectra was performed adopting 284.5 eV peak from adventitious carbon as a reference. High resolution spectra were fitted with the CasaXPS software using the U2 Tougaard background and the symmetric Voigt-like LA(1.53, 243) line shapes for peak fittings.

■ RESULTS AND DISCUSSION

Optical Microscopy and Imaging Spectroscopic Ellipsometry. Large-area 1L MoS_2 flakes were fabricated by means of a gold-assisted exfoliation technique, as detailed in the Experimental Methods. Figure 1a displays the optical microscopy image of a representative sample, showing a large, uniform monolayer with a few cracks and some multilayer or bulk-like regions. The image was obtained by stitching together 4 × 4 optical microscope frames. The 285 nm thick layer of silicon dioxide on top of the substrate enables a good optical contrast between the MoS_2 monolayer, the small multilayer areas, and the surrounding substrate.[58]

To confirm the monolayer nature of the MoS_2 crystal, we performed iSE and fitted the resulting ellipsometric data with a suitable optical model,[59] following a method presented in our previous works.[53,60,61] Figure 1b displays the thickness map of the area within the white rectangle in Figure 1a, obtained by fitting iSE data. Figure 1b shows a uniform layer of MoS_2 with a fitted average thickness of 0.7 nm, hence monolayer, with few holes and few small multilayer traces.

Laser Patterning and Time Evolution of the Photoluminescence Spectra. To obtain the desired PL enhancement, we focused a 532 nm laser to a ~2 μm circular spot, with a power density of ~0.6 MW/cm^2. The experiments were performed in air using intermittent laser irradiation to assess the nonthermal nature of the process. In particular, each irradiation cycle involved the exposure of the sample to laser light for 1 s, followed by a 59 s cool-down time. During this intermittent exposure process, PL spectra were regularly acquired by using the same optical setup used for irradiation, hence recording the time evolution of the PL peak.

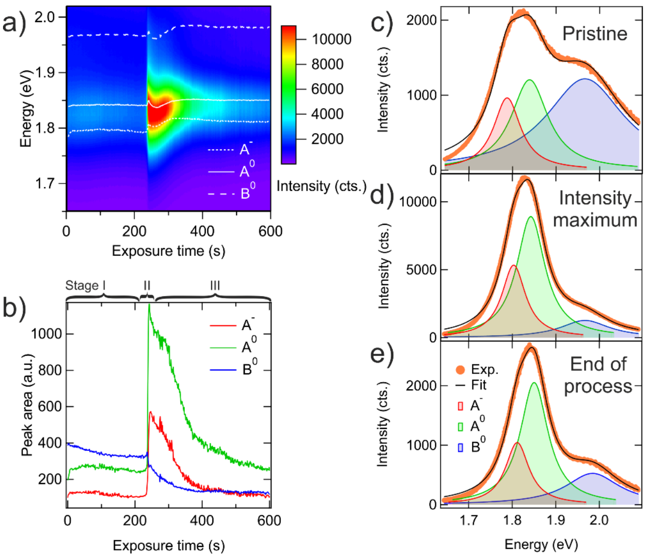

Figure 2. Time evolution of the PL spectra of 1L MoS_2 under intermittent laser exposure, with a 59 s pause after each 1 s CW exposure. a) PL spectra vs time (vertical axis: PL energy; horizontal axis: laser exposure time; color scale: PL intensity), and energy position (white traces) of the neutral A exciton (A^0), the A trion (A^-), and the B exciton (B^0). b) Time evolution of each PL-subcomponent area. Three stages of the process have been identified, and labeled in (b): an initial phase, during which no major change of the spectral line shape occurs (stage I), a sudden increase of the PL intensity (stage II), and a slow decrease of the PL intensity (stage III). c) Representative PL spectrum at the beginning of the process (stage I). There is a prominent contribution from the B exciton and an overall low PL yield. d) Representative PL spectrum at the maximum PL intensity (stage II). All peaks are blue shifted with respect to (c); the contribution from the neutral A exciton is dominant. e) PL spectrum at the end of stage III. The line shape is comparable to that of (d); however, the overall intensity is lower.

Figure 2a shows a typical evolution of PL over time. A sudden, strong increase in the PL intensity occurs after 235 min of the irradiation process, i.e., after 235 s of effective laser irradiation, since each minute corresponds only to 1 s of direct exposure. The corresponding continuous irradiation experiment, as in Figure SI1, displays analogous behavior with the PL enhancement starting after 80 s of irradiation.

Peak fitting was performed over the PL data set shown in Figure 2a to investigate the time evolution of the spectral components, i.e., the neutral A exciton (A^0), the A trion (A^-), and the B exciton (B^0). The evolution of their energy positions is plotted in Figure 2a; Figure 2b shows the evolution of the corresponding peak areas. Three stages of the enhancement process can be identified, as labeled in Figure 2b: stage I, where the PL response does not undergo any major change; stage II, where a sudden increase of the PL intensity occurs and its spectral shape changes; and stage III, where a gradual decrease in the PL intensity is observed. All peaks underwent a sharp blue shift in correspondence of stage II; afterward, the peak energy first decreased and then blue shifted again, eventually stabilizing at an energy higher than the initial value. The time evolution of stage III is included for completeness; however, laser irradiation can be stopped after stage II to obtain a higher PL.

Figure 2 panels c−e show examples of PL spectra recorded at each stage, deconvolved to identify the contributions from the neutral A exciton (A^0), the A trion (A^-), and the B exciton (B^0). In particular, Figure 2c shows the PL emission at the beginning of the process, when no enhancement had yet occurred (stage I). The overall intensity is relatively low and there is a prominent contribution from the B exciton, which is a fingerprint of a high defect density.[62] After a few minutes, during which the PL intensity remained almost unchanged, it underwent a sharp, sudden increase (stage II), followed by a gradual drop (stage III). Figure 2d shows the PL emission in correspondence of the maximum intensity, during stage II: the PL emission dramatically increased and the relative weight of the B exciton and the A^- trion were lowered. Figure 2e shows the PL emission at the end of stage III, when the overall line shape is preserved, but with lower intensity and a slightly increased B exciton contribution.

During stage I, the peak areas of the A^0 and A^- components remained rather stable, while the B exciton exhibited a slight decrease, possibly related to the desorption of physisorbed molecules under laser light. Nothing suggests any ongoing damage during this stage, despite the relatively high excitation power.

Subsequently, a sharp increase of both the A^0 exciton and the A^- trion contributions was observed, correlated with a blue shift of all three excitonic components by more than 15 meV and a decrease of the trion binding energy (defined as the energy difference between the A^0 and the A^- peaks[63]) from 53 meV during stage I to 39 meV during stage III. Notably, the B exciton contribution was not enhanced at all, hence dramatically lowering its relative weight. The apparent trion binding energies are higher than in previous reports.[64,65] This might be linked to a significant biexcitonic contribution, originating from the high excitation power.[66,67]

The reduction in the trion binding energy with a simultaneous PL enhancement is consistent with O_2 reacting with MoS_2 and acting as a p-dopant and a suppressor of nonradiative recombination sites,[26,27,68] thus providing efficient pathways for radiative recombination.[28] The exciton energies apparently red shifted after a first sharp blue shift and then slowly blue shifted again, finally stabilizing at a final energy slightly higher than the respective initial value, possibly due to subsequent evolution of the O-MoS_2 chemical bonds, which affects the charge transfer mechanism between oxygen and MoS_2. Oxygen bonding can indeed induce a screening of the Coulomb interaction, ultimately changing the exciton binding energy.[27,69,70] During stage III, a slow photoquenching affected all three components, compatible with the well-known damage process of TMDCs under high-power laser excitation.[71]

According to this picture, the presence of environmental oxygen molecules is instrumental in the laser-induced PL enhancement. In order to confirm this hypothesis, we performed an analogous process under low-vacuum conditions. In particular, the same sample was continuously exposed to laser light while kept inside a sealed Linkam THMS600 cell, held at a pressure of $\sim 10^{-1}$ mbar. Figure SI2 shows the spectra and peak fitting results for continuous exposure in low vacuum, analogous to Figure 2 for pulsed exposure in air, and to Figure SI1 for continuous exposure in air. In low vacuum, the enhancement process was significantly slower with respect to experiments performed in air, with the PL increase starting after 50 minutes of continuous irradiation. The overall PL enhancement is lower with respect to atmospheric experiments, and the spectral shifts are more contained. The degradation of the PL intensity after reaching the maximum is slower, too, as shown in Figure SI2b. This demonstrates that the ambient atmosphere plays a key role in both the enhancement process (stage II) and subsequent degradation (stage III).

Raman Spectroscopy. In order to gain further insight, Raman hyperspectral mapping was performed over a previously patterned area. The patterned spot shown in this section originates from the intermittent excitation process shown in Figure 2a, and was measured after the end of stage III.

Figure 3a shows representative Raman spectra at the edge, at the center, and in a pristine area, in the spectral region of the E' and A_1' peaks. These peaks in monolayer MoS_2 (point group D_{3h}) correspond to the E_{2g}^1 and A_{1g} modes in bulk MoS_2 (point group D_{6h}).[72−74] It is apparent that the central area shows no Raman signal; both the edge of the pattern and the pristine area display identical E_{2g} peaks, albeit with distinct A_1' peaks. The full Raman spectra are shown in Figure SI3. To investigate the local behavior of the Raman peaks, spectral fitting was performed with two Lorentzian components, corresponding to the E' mode at 385 cm^{-1} and A_1' modes at 405 cm^{-1}. The energy shift between the two peaks unambiguously confirms the monolayer nature of the MoS_2 film, as the separation between the E' and the A_1' Raman modes is a fingerprint of the number of layers.[75,76] Raman shift and intensity maps for the aforementioned modes are shown in Figure 3b−e. The central region of the irradiated area shows no trace of the MoS_2 Raman peaks due to a complete ablation of the material. In the surrounding area, the E' mode shows no relevant intensity pattern, whereas the A_1' exhibits a prominent intensity increase over an annular area around the circular ablated hole. Similarly, the E' mode undergoes no relevant shift, whereas the A_1' mode blue shifts by ~ 0.5 cm^{-1} with respect to the pristine area. It is worth noting that the E' mode is more sensitive to strain, while the A_1' mode is more sensitive to doping.[77,78] Indeed, the blue shift of the A_1' mode, with the E' mode unaffected, is a clear fingerprint of p-type doping,[27,78−80] suggesting that the PL enhancement process is accompanied by a local change in the doping level, as already suggested by the time evolution of the PL spectra and further confirmed by the spatially resolved PL investigation presented in the next section. Notably, Rao et al. observed a similar evolution of the Raman peaks under low-power laser irradiation, which they attributed to oxygen passivation of chalcogen vacancies leading to p-type doping.[81]

Raman shifts can be used to estimate strain and doping levels.[72,82−85] A correlative plot of the Raman peak positions is shown in Figure SI4, revealing a narrow dispersion of the E' mode, associated with strain, and a pronounced blue shift of the A_1' mode for points closer to the spot center, consistent with p-

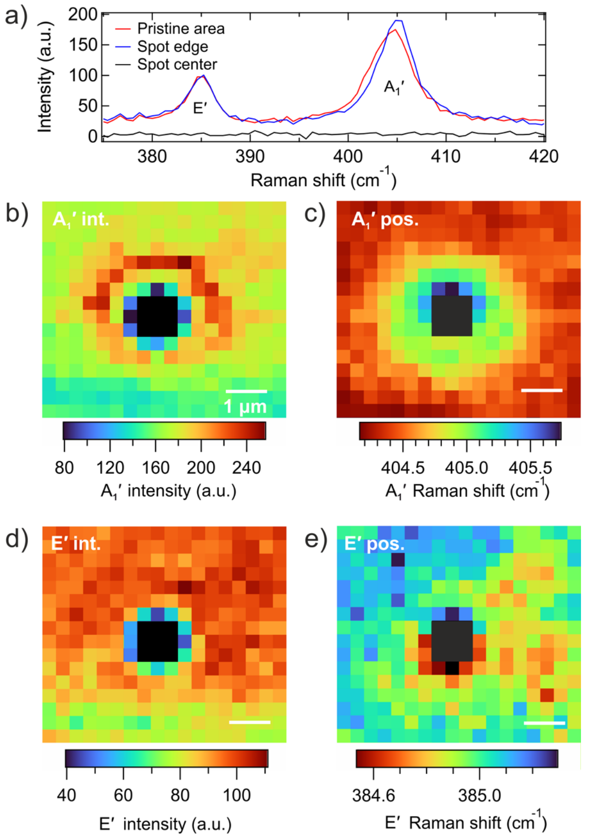

Figure 3. Raman mapping of the E′ and A$_1'$ modes over a patterned spot. a) Raman spectra of representative points: at the edge of the patterned spot, at its center, and over a pristine area. The central area shows no Raman signal. The pattern edge and the pristine area show identical E′ peaks, whereas the A$_1'$ peak is higher and blue shifted on the spot edge with respect to the pristine area. b) Peak intensity of the A$_1'$ mode, showing a local enhancement on the edges of the spot and no Raman signal from its center. c) Raman shift of the A$_1'$ mode, showing a notable blue shift around the patterned spot. d) Peak intensity of the E′ mode, showing no significant intensity pattern. e) Raman shift of the E′ mode, showing no relevant peak shift.

type doping. Following the assumptions adopted in ref 72, the electron density near the spot edges and in the pristine area is estimated to be -3×10^{11} cm^{-2} (p-type doping) and 3×10^{12} cm^{-2} (n-type doping), respectively, as detailed in Section SI4.

Tip-Enhanced Photoluminescence Spectroscopy. The Raman mapping already suggests that different subregions with different properties are present on irradiated samples. In order to probe the optical response with high lateral resolution, TEPL was performed to investigate the observed local enhancement of the PL. Indeed, TEPL allows overcoming Abbe's diffraction limit and resolve lateral features smaller than the light wavelength.[86]

TEPL measurements were performed on a spot previously patterned by continuous irradiation in air under the same experimental conditions of the process shown in Figure SI1. For these experiments, laser exposure was stopped during stage III, when the intensity was approximately halved with respect to the maximum achieved during stage II.

Figure 4a shows the TEPL intensity map over the patterned area. It is apparent that the TEPL enhancement occurs on an annular area with micrometric size, whereas the central region provides little to no PL signal and the surrounding area provides the same PL signal as that of a pristine monolayer. Figure 4b displays a high resolution TEPL intensity map across the annular profile shown in Figure 4a, clarifying that the high-PL area is an ∼300 nm wide streak. The spatially averaged PL spectra, corresponding to representative areas in Figure 4b (labeled 1, 2, and 3), are reported in Figure 4c−e, respectively. We note that PL spectra shown in Figure 4c−e were acquired under moderate excitation intensity, whereas spectra shown in Figure 2c−e were acquired under high-power excitation to achieve V_S healing, and high laser intensity is known to alter the PL line shape.[65,87] Moreover, TEPL may alter the PL line shape, in particular at longer wavelengths.[88]

The spectra were fitted with two Lorentzian components, corresponding to neutral exciton A^0 and trion A^-.

It is apparent that the relative weight and the width of the exciton and trion components change as a function of the radial distance from the laser spot. Table 1 summarizes the fit results. The energy of the neutral exciton remains stable, whereas the trion blue shifts in the regions with enhanced PL (regions 1 and 2). Moreover, the enhanced PL regions feature a lower FWHM for both the components and a lower weight of the trion component.

AFM images of the same patterned region investigated by TEPL are shown in Figure SI5, revealing that the MoS_2 layer was ablated by the laser in a circular spot, while the pattern edges exhibit no morphological modifications. Experimental observations suggest that ablation occurs at the beginning of stage II and that no enhancement can be observed before the formation of a hole.

XPS Microscopy. To investigate the chemical processes underlying the PL enhancement, the chemical state of 1L MoS_2 under both the pristine and laser-exposed conditions was investigated by means of spatially resolved XPS measurements. Details about data acquisition and processing are available in the Experimental Methods section and in Supporting Information section SI6.

A MoS_2 crystal was patterned with a square 5 × 5 hole array consisting of 25 equally spaced laser-irradiated spots, the centers of which are 5 μm apart from each other. The decision to pattern a hole array rather than a single hole is purely technical, motivated by the necessity to have a relatively large area with a large density of laser-processed regions. Laser patterning was performed in air under continuous laser exposure. After patterning, all of the spots in the pattern showed the typical PL enhancement behavior, with high PL emission from annular regions corresponding to the edge of each spot (Figure 6d).

XPS spectra were acquired with a 9 μm diameter X-ray spot, while chemical mapping was performed with a 150 nm spot for high spatial resolution. Spectra of the Mo 3d and S 2p peaks over a 9 μm circular area centered over one of the 25 patterned spots are shown in the upper half of Figure 5a,b, respectively. The lower half of the same figure provides a direct comparison with the corresponding spectra on a nearby pristine monolayer area. Both the patterned and the pristine areas show a prominent Mo $3p_{5/2}/3p_{3/2}$ doublet with a binding energy (BE) of 229.3 eV/232.5 eV, clearly originating from the MoS_2 layer, and accordingly ascribed to Mo(IV) states in MoS_2.[89−93] A further Mo 3p doublet with higher BE, located at 230.6 eV/233.8 eV can be observed only in the patterned area and can be ascribed to Mo(V) states.[94] This doublet is attributed to mixed compounds of molybdenum, oxygen, and sulfur[95] belonging to the patterned edges. Any Mo(VI) states, such as those in MoO_3 commonly reported at BEs around 232.7 eV,[96,97] would account for less

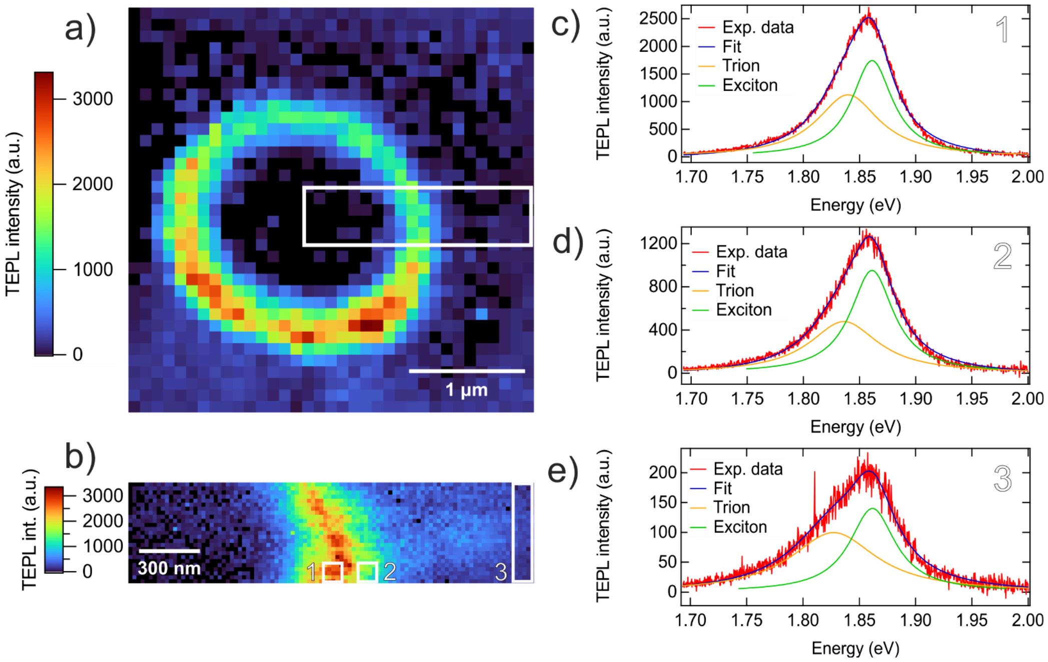

Figure 4. High resolution TEPL imaging and spectral analysis of a patterned spot. a) TEPL intensity over a 3.5 × 3.5 μm^2 area around a patterned spot. The map shows the maximum intensity of the spectra acquired at each spatial point. b) Zoom over a 2 × 0.5 μm^2 area of the map shown in (a). c) spectral average corresponding to zone 1 as marked in panel b, representing the maximum PL enhancement. d) spectral average corresponding to zone 2 as marked in panel b, representing medium PL enhancement. e) spectral average corresponding to zone 3 as marked in panel b, representing pristine MoS_2.

Table 1. PL Fitting Results from the Regions Marked in Figure 4b

Region	E_{exc} (eV)	E_{trion} (eV)	$FWHM_{exc}$ (meV)	$FWHM_{trion}$ (meV)	$Area_{trion}/Area_{exc}$
1	1.861 ± 0.001	1.840 ± 0.002	44 ± 2	68 ± 2	1.0 ± 0.2
2	1.861 ± 0.001	1.836 ± 0.003	47 ± 2	75 ± 3	0.8 ± 0.2
3	1.862 ± 0.001	1.827 ± 0.004	49 ± 3	92 ± 6	1.3 ± 0.3

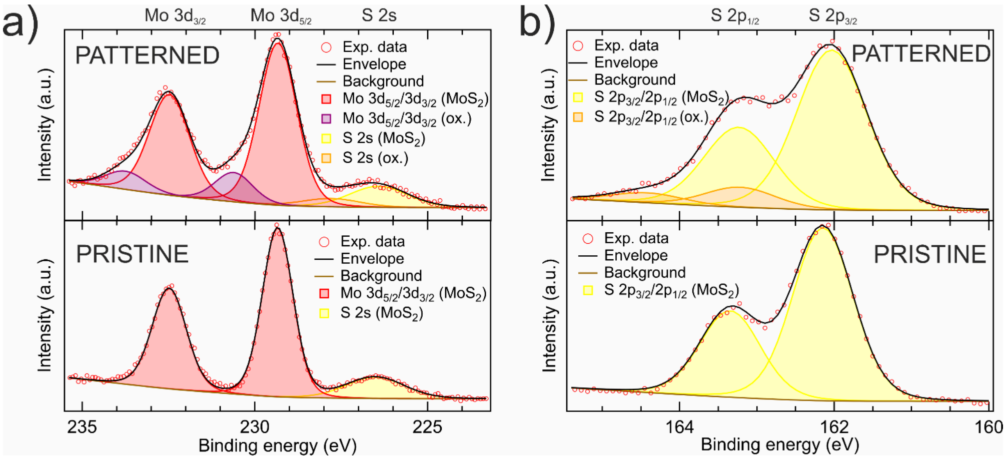

Figure 5. a) Spectra of the Mo 3d/S 2s XPS peaks from a 9 μm o.d. area centered on a patterned spot (upper panel) and on a pristine area (lower panel). Both areas show a prominent Mo(IV) doublet from the MoS_2 monolayer. The patterned area shows an additional Mo doublet related to Mo(V) states. b) Spectra of the S 2p XPS peak over the same spots. In addition to the prominent S doublet linked to the MoS_2 layer, the patterned area shows a second doublet with higher BE.

than 3% of the total Mo contribution and are not included in this fitting.

XPS spectra of the S 2p region, shown in Figure 5b, exhibit a prominent S $2p_{3/2}/2p_{1/2}$ doublet with BEs of 162.1 and 163.3 eV, respectively, as expected for MoS_2.[90,93] On the patterned spot, a further doublet at 163.2 and 164.4 eV can be observed. Consistent with the Mo case, this doublet can be linked to the presence of molybdenum oxysulfides.[95] Indeed, elemental sulfur or sulfates would be located at higher BEs.[98,99] Given the increased width of the S 2p peaks in the patterned region, we cannot exclude the presence of further sulfur states linked to the oxidation process. Concerning the oxygen peaks, the contribu-

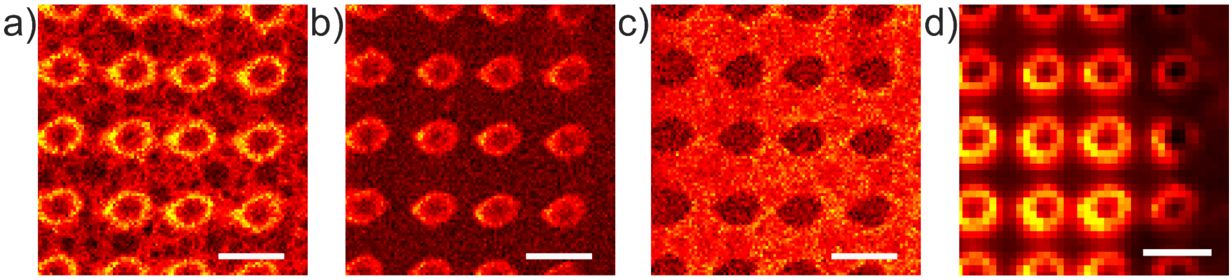

Figure 6. XPS Mo 3d$_{5/2}$ intensity maps and comparison with the PL response. Brighter colors correspond to higher intensities. Scale bars: 5 μm. a) Map of the Mo 3d$_{5/2}$ chemical distribution over an array of laser-patterned spots. The XPS signal is higher on annular regions corresponding to the edges of each spot. b) Intensity map of the higher BE subcomponent of the Mo 3d$_{5/2}$ XPS peak, clearly localized on the edges of each spot. c) Intensity map of the lower BE subcomponent of the Mo 3d$_{5/2}$ XPS peak, showing uniform intensity over the untreated MoS$_2$ area and not changing over the edges of the spots. d) Map of the PL peak height over the same area.

tion from the underlying SiO$_2$ layer limits the extent to which they can be meaningfully interpreted.

Figure 6a shows the Mo 3d$_{5/2}$ chemical distribution. This mapping was performed at high lateral resolution and low spectral resolution over an array of laser-exposed spots with 5 μm pitch. The analysis procedure is detailed in Supporting Information section SI6. Figure 6 panels b and c depict the higher and lower BE contributions to the Mo 3d peak, respectively. Figure 6d shows the PL peak area over the same zone. The PL intensity behavior correlates very well with the structures observed in the chemical maps. An annular region around each spot shows an enhanced PL emission, where a more intense Mo 3d$_{5/2}$ peak is observed. Figure 6 panels b and c highlight how the enhancement is associated with the appearance of the high-BE component of the Mo 3d peak already seen in the high-resolution XPS spectra. The low-BE component (Figure 6c) is uniform over the whole area and simply disappears within the holes due to MoS$_2$ ablation. On the contrary, the high-BE component (Figure 6b) is prominent on the annular regions corresponding to the high-PL areas. These two maps complement the spatially averaged high-resolution spectral analysis shown in Figure 5, demonstrating that the high-BE Mo 3d peaks observed in high-resolution spectra originate from the annular edge of the patterned spot.

Putting all the evidence together, we suggest the following model for the laser-induced PL enhancement. We start from the evidence that the pristine layers employed in this study house a certain amount of defects (V_S) that give rise to a superposition of A-exciton, trion, and B exciton in the original PL spectrum. The collected data and literature suggest that the oxidation at V_S sites promotes an increase of the neutral A exciton emission, a decrease of the B exciton and A$^-$ trion emission, a decrease of the trion binding energy, and a blue shift of the A$_1'$ Raman peak. Notably, O-substituted V_S do not introduce states in the bandgap, whereas single V_S and paired V_S are associated with one (at 440 meV below the conduction band) and two (at 303 and 633 meV below the conduction band) bandgap states, respectively.[100−103] Our experiments indicate that such an oxidized region, under the above specified irradiation conditions, has an annular shape concentric with the laser spot. We suggest that the system dynamics under laser irradiation is the following. Laser exposure induces a nonequilibrium state that increases the reactivity of MoS$_2$. In correspondence with the highest irradiation intensity (at the spot center), the TMDC, probably after reacting with atmospheric oxygen, is locally ablated. The ablation edges possess increased reactivity, and the ablation spot, once created, quickly enlarges, leading to more oxidation and more ablation. The ablation stops once the MoS$_2$ ablated edge reaches the edges of the spot, where the laser intensity becomes insufficient to sustain more photoinduced reaction, and hence more ablation. This leaves behind an ablated spot and an annular region where V_S are healed by photoinduced oxidation and, outside this region, the pristine monolayer. Evidence of the correlation between the PL emission and this oxygen-healed state is coherently provided by Raman spectroscopy (blue shift of the A$_1'$ peak), AFM (ablated spot and absence of morphological features in the annular region) and XPS (appearance of additional Mo and S chemical bonds), all with spatial resolution. All of these results consistently indicate a defect-healing phenomenon associated with p-type counterdoping due to laser-induced oxygen bonding at V_S sites.

■ CONCLUSIONS

This work investigates the mechanism of the laser-induced PL enhancement of 1L MoS$_2$. The most evident result is an increase of the PL intensity by up to 1 order of magnitude with respect to the untreated area. A comprehensive investigation of the phenomenon allowed clarifying that the process relies on ambient air exposure and it is not a purely thermal process induced by laser-induced heating. The observed enhancement is associated with a sharp shift from trion to exciton emission, a strong reduction of the B exciton emission, and a blue shift of all PL peaks. The high lateral resolution enabled by TEPL spectroscopy made it clear that the enhanced PL emission comes from the very edge of a micrometric hole created on the TMDC monolayer by the laser beam, as confirmed by AFM imaging. Raman analysis and TEPL fitting consistently show the PL enhancement phenomenon is associated with a p-type counterdoping of the interested region, with a blue shift of the A$_1'$ Raman mode and a blue shift of the trion PL peak. A local chemical investigation through XPS analysis with high lateral resolution and imaging capabilities allowed linking this enhancement with laser-induced oxidation of the V_S at the edge of the hole.[34,69,79,104] We note that no enhancement was observed without hole formation; this could be a limiting factor for the large-scale exploitation of this phenomenon for defect healing. The prolonged laser exposure (stage I) may create additional defects, allowing them to reach a critical density at which a sudden breakage of the monolayer occurs, exposing dangling bonds that rapidly bind to oxygen. The reaction stops at the edge of the laser spot, where the light intensity becomes insufficient to continue it.

These results help us to understand the role of defects in 2D TMDCs and underline how their interplay with intense light beams, be it intentional or accidental, can lead to local, yet extremely significant, modifications in their chemical, electronic, and optical features. The observed PL enhancement can be exploited to locally tailor the properties of 2D TMDCs in any application where a clear, localized spectral feature can be exploited as an optically readable marker.

■ ASSOCIATED CONTENT

Supporting Information

The Supporting Information is available free of charge at https://pubs.acs.org/doi/10.1021/acs.jpcc.5c05608.

> Evolution of the PL peak during continuous exposure in air; evolution of the PL peak during continuous exposure in low vacuum; Raman spectra; Raman peak analysis; atomic force microscopy; spatially resolved XPS analysis (PDF)

■ AUTHOR INFORMATION

Corresponding Author

Ermes Peci – *OptMatLab, Dipartimento di Fisica, Università di Genova, 16146 Genova, Italy;* orcid.org/0000-0001-8536-3705; Email: ermes.peci@edu.unige.it

Authors

Yang Pan – *Semiconductor Physics and Center for Materials, Architectures and Integration of Nanomembranes (MAIN), Chemnitz University of Technology, D-09107 Chemnitz, Germany;* orcid.org/0000-0003-4902-8197
Emma Spotorno – *OptMatLab, Dipartimento di Fisica, Università di Genova, 16146 Genova, Italy;* orcid.org/0009-0001-9544-4645
Lorenzo Ramò – *OptMatLab, Dipartimento di Fisica, Università di Genova, 16146 Genova, Italy;* orcid.org/0000-0001-7008-7226
Francesca Telesio – *Dipartimento di Fisica, Università di Genova, 16146 Genova, Italy*
Michele Magnozzi – *OptMatLab, Dipartimento di Fisica, Università di Genova, 16146 Genova, Italy*
Zygmunt Miłosz – *Elettra Sincrotrone Trieste S.C.p.A., 34149 Trieste, Italy;* orcid.org/0000-0002-4938-9331
Luca Gregoratti – *Elettra Sincrotrone Trieste S.C.p.A., 34149 Trieste, Italy*
Matteo Amati – *Elettra Sincrotrone Trieste S.C.p.A., 34149 Trieste, Italy*
Nicolò Petrini – *Politecnico di Torino, 10129 Torino, Italy*
Ilka Kriegel – *Politecnico di Torino, 10129 Torino, Italy;* orcid.org/0000-0002-0221-3769
Dietrich R. T. Zahn – *Semiconductor Physics and Center for Materials, Architectures and Integration of Nanomembranes (MAIN), Chemnitz University of Technology, D-09107 Chemnitz, Germany;* orcid.org/0000-0002-8455-4582
Maurizio Canepa – *OptMatLab, Dipartimento di Fisica, Università di Genova, 16146 Genova, Italy;* orcid.org/0000-0002-5148-1233
Francesco Bisio – *CNR-SPIN, 16152 Genova, Italy;* orcid.org/0000-0003-1776-3023

Complete contact information is available at:
https://pubs.acs.org/10.1021/acs.jpcc.5c05608

Notes

The authors declare no competing financial interest.

■ ACKNOWLEDGMENTS

The research leading to these results received funding from the Ministero dell'Istruzione, dell'Università e della Ricerca: Dipartimenti di Eccellenza 2018–2022 and PRIN 2017 no. 2017KFY7XF. We acknowledge Elettra Sincrotrone Trieste for providing access to its synchrotron radiation facilities and for financial support under the SUI internal project.

■ REFERENCES

(1) Novoselov, K. S.; Mishchenko, A.; Carvalho, A.; Castro Neto, A. 2D Materials and van der Waals heterostructures. *Science* **2016**, *353*, aac9439.

(2) Manzeli, S.; Ovchinnikov, D.; Pasquier, D.; Yazyev, O. V.; Kis, A. 2D transition metal dichalcogenides. *Nat. Rev. Mater.* **2017**, *2*, 17033.

(3) Splendiani, A.; Sun, L.; Zhang, Y.; Li, T.; Kim, J.; Chim, C.-Y.; Galli, G.; Wang, F. Emerging photoluminescence in monolayer MoS_2. *Nano Lett.* **2010**, *10*, 1271–1275.

(4) Jie, W.; Yang, Z.; Bai, G.; Hao, J. Luminescence in 2D Materials and van der Waals Heterostructures. *Adv. Opt. Mater.* **2018**, *6*, 1701296.

(5) Mueller, T.; Malic, E. Exciton physics and device application of two-dimensional transition metal dichalcogenide semiconductors. *npj 2D Mater. Appl.* **2018**, *2*, 29.

(6) Chernikov, A.; Berkelbach, T. C.; Hill, H. M.; Rigosi, A.; Li, Y.; Aslan, B.; Reichman, D. R.; Hybertsen, M. S.; Heinz, T. F. Exciton binding energy and nonhydrogenic Rydberg series in monolayer WS_2. *Phys. Rev. Lett.* **2014**, *113*, 076802.

(7) Chaves, A.; Azadani, J. G.; Alsalman, H.; da Costa, D. R.; Frisenda, R.; Chaves, A. J.; Song, S. H.; Kim, Y. D.; He, D.; Zhou, J.; et al. Bandgap engineering of two-dimensional semiconductor materials. *npj 2D Mater. Appl.* **2020**, *4*, 29.

(8) Raja, A.; Chaves, A.; Yu, J.; Arefe, G.; Hill, H. M.; Rigosi, A. F.; Berkelbach, T. C.; Nagler, P.; Schüller, C.; Korn, T.; et al. Coulomb engineering of the bandgap and excitons in two-dimensional materials. *Nat. Commun.* **2017**, *8*, 15251.

(9) Mak, K. F.; He, K.; Shan, J.; Heinz, T. F. Control of valley polarization in monolayer MoS_2 by optical helicity. *Nat. Nanotechnol.* **2012**, *7*, 494–498.

(10) Schaibley, J. R.; Yu, H.; Clark, G.; Rivera, P.; Ross, J. S.; Seyler, K. L.; Yao, W.; Xu, X. Valleytronics in 2D Materials. *Nat. Rev. Mater.* **2016**, *1*, 16055.

(11) Psilodimitrakopoulos, S.; Mouchliadis, L.; Paradisanos, I.; Kourmoulakis, G.; Lemonis, A.; Kioseoglou, G.; Stratakis, E. Twist angle mapping in layered WS_2 by polarization-resolved second harmonic generation. *Sci. Rep.* **2019**, *9*, 14285.

(12) Li, Y.; Rao, Y.; Mak, K. F.; You, Y.; Wang, S.; Dean, C. R.; Heinz, T. F. Probing symmetry properties of few-layer MoS_2 and h-BN by optical second-harmonic generation. *Nano Lett.* **2013**, *13*, 3329–3333.

(13) Yin, Z.; Li, H.; Li, H.; Jiang, L.; Shi, Y.; Sun, Y.; Lu, G.; Zhang, Q.; Chen, X.; Zhang, H. Single-layer MoS_2 phototransistors. *ACS Nano* **2012**, *6*, 74–80.

(14) Wang, Z.; Jingjing, Q.; Wang, X.; Zhang, Z.; Chen, Y.; Huang, X.; Huang, W. Two-dimensional light-emitting materials: preparation, properties and applications. *Chem. Soc. Rev.* **2018**, *47*, 6128–6174.

(15) Ye, Y.; Wong, Z. J.; Lu, X.; Ni, X.; Zhu, H.; Chen, X.; Wang, Y.; Zhang, X. Monolayer excitonic laser. *Nat. Photonics* **2015**, *9*, 733–737.

(16) Jariwala, D.; Sangwan, V. K.; Lauhon, L. J.; Marks, T. J.; Hersam, M. C. Emerging device applications for semiconducting two-dimensional transition metal dichalcogenides. *ACS Nano* **2014**, *8*, 1102–1120.

(17) Liang, Q.; Zhang, Q.; Zhao, X.; Liu, M.; Wee, A. T. Defect engineering of two-dimensional transition-metal dichalcogenides: applications, challenges, and opportunities. *ACS Nano* **2021**, *15*, 2165–2181.

(18) Hu, Z.; Wu, Z.; Han, C.; He, J.; Ni, Z.; Chen, W. Two-dimensional transition metal dichalcogenides: interface and defect engineering. *Chem. Soc. Rev.* **2018**, *47*, 3100–3128.

(19) Yuan, L.; Huang, L. Exciton dynamics and annihilation in WS_2 2D semiconductors. *Nanoscale* **2015**, *7*, 7402–7408.

(20) Wang, H.; Zhang, C.; Rana, F. Ultrafast dynamics of defect-assisted electron−hole recombination in monolayer MoS_2. *Nano Lett.* **2015**, *15*, 339−345.

(21) Li, Z.; Bretscher, H.; Zhang, Y.; Delport, G.; Xiao, J.; Lee, A.; Stranks, S. D.; Rao, A. Mechanistic insight into the chemical treatments of monolayer transition metal disulfides for photoluminescence enhancement. *Nat. Commun.* **2021**, *12*, 6044.

(22) Amani, M.; Lien, D.-H.; Kiriya, D.; Xiao, J.; Azcatl, A.; Noh, J.; Madhvapathy, S. R.; Addou, R.; KC, S.; Dubey, M.; et al. Near-unity photoluminescence quantum yield in MoS_2. *Science* **2015**, *350*, 1065−1068.

(23) Addou, R.; McDonnell, S.; Barrera, D.; Guo, Z.; Azcatl, A.; Wang, J.; Zhu, H.; Hinkle, C. L.; Quevedo-Lopez, M.; Alshareef, H. N.; et al. Impurities and electronic property variations of natural MoS_2 crystal surfaces. *ACS Nano* **2015**, *9*, 9124−9133.

(24) Hong, J.; Hu, Z.; Probert, M.; Li, K.; Lv, D.; Yang, X.; Gu, L.; Mao, N.; Feng, Q.; Xie, L.; et al. Exploring atomic defects in molybdenum disulphide monolayers. *Nat. Commun.* **2015**, *6*, 6293.

(25) Lin, Z.; Carvalho, B. R.; Kahn, E.; Lv, R.; Rao, R.; Terrones, H.; Pimenta, M. A.; Terrones, M. Defect engineering of two-dimensional transition metal dichalcogenides. *2D Mater.* **2016**, *3*, 022002.

(26) Tongay, S.; Zhou, J.; Ataca, C.; Liu, J.; Kang, J. S.; Matthews, T. S.; You, L.; Li, J.; Grossman, J. C.; Wu, J. Broad-range modulation of light emission in two-dimensional semiconductors by molecular physisorption gating. *Nano Lett.* **2013**, *13*, 2831−2836.

(27) Nan, H.; Wang, Z.; Wang, W.; Liang, Z.; Lu, Y.; Chen, Q.; He, D.; Tan, P.; Miao, F.; Wang, X.; et al. Strong photoluminescence enhancement of MoS_2 through defect engineering and oxygen bonding. *ACS Nano* **2014**, *8*, 5738−5745.

(28) Shu, H.; Li, Y.; Niu, X.; Wang, J. Greatly enhanced optical absorption of a defective MoS_2 monolayer through oxygen passivation. *ACS Appl. Mater. Interfaces* **2016**, *8*, 13150−13156.

(29) Kiriya, D.; Lien, D.-H. Superacid Treatment on Transition Metal Dichalcogenides. *Nano Express* **2022**, *3*, 034002.

(30) Bretscher, H.; Li, Z.; Xiao, J.; Qiu, D. Y.; Refaely-Abramson, S.; Alexander-Webber, J. A.; Tanoh, A.; Fan, Y.; Delport, G.; Williams, C. A.; et al. Rational passivation of sulfur vacancy defects in two-dimensional transition metal dichalcogenides. *ACS Nano* **2021**, *15*, 8780−8789.

(31) Feng, Q.; Sun, Y.; Li, Y.; Yan, J.; Zhong, W.; Yang, G.; Liu, W.; Xu, H.; Liu, Y. Highly photoluminescent monolayer MoS_2 and WS_2 achieved via superacid assisted vacancy reparation and doping strategy. *Laser Photonics Rev.* **2021**, *15*, 2100104.

(32) Healy, B. F. M.; Pain, S. L.; Lloyd-Hughes, J.; Grant, N. E.; Murphy, J. D. Tunable Photoluminescence from Monolayer Molybdenum Disulfide. *Adv. Mater. Interfaces* **2024**, *11*, 2400305.

(33) Pain, S. L.; Grant, N. E.; Murphy, J. D. Room Temperature Enhancement of Electronic Materials by Superacid Analogues. *ACS Nano* **2022**, *16*, 1260−1270.

(34) Zhang, X.; Liao, Q.; Liu, S.; Kang, Z.; Zhang, Z.; Du, J.; Li, F.; Zhang, S.; Xiao, J.; Liu, B.; et al. Poly (4-styrenesulfonate)-induced sulfur vacancy self-healing strategy for monolayer MoS_2 homojunction photodiode. *Nat. Commun.* **2017**, *8*, 15881.

(35) Lien, D.-H.; Uddin, S. Z.; Yeh, M.; Amani, M.; Kim, H.; Ager III, J. W.; Yablonovitch, E.; Javey, A. Electrical suppression of all nonradiative recombination pathways in monolayer semiconductors. *Science* **2019**, *364*, 468−471.

(36) Mouri, S.; Miyauchi, Y.; Matsuda, K. Tunable photoluminescence of monolayer MoS_2 via chemical doping. *Nano Lett.* **2013**, *13*, 5944−5948.

(37) Han, H.-V.; Lu, A.-Y.; Lu, L.-S.; Huang, J.-K.; Li, H.; Hsu, C.-L.; Lin, Y.-C.; Chiu, M.-H.; Suenaga, K.; Chu, C.-W.; et al. Photoluminescence enhancement and structure repairing of monolayer $MoSe_2$ by hydrohalic acid treatment. *ACS Nano* **2016**, *10*, 1454−1461.

(38) Kim, S. Y.; Yang, H. I.; Choi, W. Photoluminescence quenching in monolayer transition metal dichalcogenides by Al_2O_3 encapsulation. *Appl. Phys. Lett.* **2018**, *113*, 133104.

(39) Li, Y.; Li, X.; Chen, H.; Shi, J.; Shang, Q.; Zhang, S.; Qiu, X.; Liu, Z.; Zhang, Q.; Xu, H.; et al. Controlled Gas Molecules Doping of Monolayer MoS_2 via Atomic-Layer-Deposited Al_2O_3 Films. *ACS Appl. Mater. Interfaces* **2017**, *9*, 27402−27408.

(40) Harats, M. G.; Kirchhof, J. N.; Qiao, M.; Greben, K.; Bolotin, K. I. Dynamics and efficient conversion of excitons to trions in non-uniformly strained monolayer WS_2. *Nat. Photonics* **2020**, *14*, 324−329.

(41) Waheed, Y.; Shit, S.; Surendran, J. T.; Prasad, I. D.; Watanabe, K.; Taniguchi, T.; Kumar, S. Large trion binding energy in monolayer WS_2 via strain-enhanced electron−phonon coupling. *Commun. Mater.* **2025**, *6*, 86.

(42) Vaquero, D.; Clericò, V.; Salvador-Sánchez, J.; Martín-Ramos, A.; Díaz, E.; Domínguez-Adame, F.; Meziani, Y. M.; Diez, E.; Quereda, J. Excitons, trions and Rydberg states in monolayer MoS_2 revealed by low-temperature photocurrent spectroscopy. *Commun. Phys.* **2020**, *3*, 194.

(43) Pan, Y.; Rahaman, M.; He, L.; Milekhin, I.; Manoharan, G.; Aslam, M. A.; Blaudeck, T.; Willert, A.; Matković, A.; Madeira, T. I.; et al. Exciton tuning in monolayer WSe_2 via substrate induced electron doping. *Nanoscale Adv.* **2022**, *4*, 5102−5108.

(44) H L, P.; Mondal, P.; Bid, A.; Basu, J. K. Electrical and Chemical Tuning of Exciton Lifetime in Monolayer MoS_2 for Field-Effect Transistors. *ACS Appl. Nano Mater.* **2020**, *3*, 641−647.

(45) Kesarwani, R.; Simbulan, K. B.; Huang, T.-D.; Chiang, Y.-F.; Yeh, N.-C.; Lan, Y.-W.; Lu, T.-H. Control of trion-to-exciton conversion in monolayer WS_2 by orbital angular momentum of light. *Sci. Adv.* **2022**, *8*, No. eabm0100.

(46) Lu, J.; Carvalho, A.; Chan, X. K.; Liu, H.; Liu, B.; Tok, E. S.; Loh, K. P.; Castro Neto, A.; Sow, C. H. Atomic healing of defects in transition metal dichalcogenides. *Nano Lett.* **2015**, *15*, 3524−3532.

(47) Hou, C.; Deng, J.; Guan, J.; Yang, Q.; Yu, Z.; Lu, Y.; Xu, Z.; Yao, Z.; Zheng, J. Photoluminescence of monolayer MoS_2 modulated by water/O_2/laser irradiation. *Phys. Chem. Chem. Phys.* **2021**, *23*, 24579−24588.

(48) Oh, H. M.; Han, G. H.; Kim, H.; Bae, J. J.; Jeong, M. S.; Lee, Y. H. Photochemical reaction in monolayer MoS_2 via correlated photoluminescence, Raman spectroscopy, and MoS_2 force microscopy. *ACS Nano* **2016**, *10*, 5230−5236.

(49) Xie, H.; Liu, C.; Hu, H.; Yin, H.; Zhong, J.; Zong, X.; Jiang, X.; Zhang, J.; Wang, W.; Tao, Y.; et al. Evolutional photoluminescence property in ultraviolet-ozone-treated monolayer MoS_2. *Appl. Surf. Sci.* **2021**, *545*, 148809.

(50) Bera, A.; Muthu, D.; Sood, A. Enhanced Raman and photoluminescence response in monolayer MoS_2 due to laser healing of defects. *J. Raman Spectrosc.* **2018**, *49*, 100−105.

(51) Venkatakrishnan, A.; Chua, H.; Tan, P.; Hu, Z.; Liu, H.; Liu, Y.; Carvalho, A.; Lu, J.; Sow, C. H. Microsteganography on WS_2 monolayers tailored by direct laser painting. *ACS Nano* **2017**, *11*, 713−720.

(52) Abyaneh, M. K.; Gregoratti, L.; Amati, M.; Dalmiglio, M.; Kiskinova, M. Scanning photoelectron microscopy: a powerful technique for probing micro and nano-structures. *E-J. Surf. Sci. Nanotechnol.* **2011**, *9*, 158−162.

(53) Petrini, N.; Peci, E.; Curreli, N.; Spotorno, E.; Kazemi Tofighi, N.; Magnozzi, M.; Scotognella, F.; Bisio, F.; Kriegel, I. Optimizing Gold-Assisted Exfoliation of Layered Transition Metal Dichalcogenides with (3-Aminopropyl)triethoxysilane (APTES): A Promising Approach for Large-Area Monolayers. *Adv. Opt. Mater.* **2024**, *12*, 2303228.

(54) Velický, M.; Donnelly, G. E.; Hendren, W. R.; McFarland, S.; Scullion, D.; DeBenedetti, W. J. I.; Correa, G. C.; Han, Y.; Wain, A. J.; Hines, M. A.; et al. Mechanism of Gold-Assisted Exfoliation of Centimeter-Sized Transition-Metal Dichalcogenide Monolayers. *ACS Nano* **2018**, *12*, 10463−10472.

(55) Rahaman, M.; Selyshchev, O.; Pan, Y.; Schwartz, R.; Milekhin, I.; Sharma, A.; Salvan, G.; Gemming, S.; Korn, T.; Zahn, D. R. T. Observation of Room-Temperature Dark Exciton Emission in Nanopatch-Decorated Monolayer WSe_2 on Metal Substrate. *Adv. Opt. Mater.* **2021**, *9*, 2101801.

(56) Rahaman, M.; Marino, E.; Joly, A. G.; Stevens, C. E.; Song, S.; Alfieri, A.; Jiang, Z.; O'Callahan, B. T.; Rosen, D. J.; Jo, K.; et al. Tunable

https://doi.org/10.1021/acs.jpcc.5c05608

Localized Charge Transfer Excitons in Nanoplatelet−2D Chalcogenide van der Waals Heterostructures. *ACS Nano* **2024**, *18*, 15185−15193.

(57) Gregoratti, L.; Barinov, A.; Benfatto, E.; Cautero, G.; Fava, C.; Lacovig, P.; Lonza, D.; Kiskinova, M.; Tommasini, R.; Mähl, S.; et al. 48-Channel electron detector for photoemission spectroscopy and microscopy. *Rev. Sci. Instrum.* **2004**, *75*, 64−68.

(58) Li, H.; Wu, J.; Huang, X.; Lu, G.; Yang, J.; Lu, X.; Xiong, Q.; Zhang, H. Rapid and reliable thickness identification of two-dimensional nanosheets using optical microscopy. *ACS Nano* **2013**, *7*, 10344−10353.

(59) Peci, E.; Magnozzi, M.; Ramò, L.; Ferrera, M.; Convertino, D.; Pace, S.; Orlandini, G.; Sharma, A.; Milekhin, I.; Salvan, G.; et al. Dielectric Function of 2D Tungsten Disulfide in Homo- and Heterobilayer Stacking. *Adv. Mater. Interfaces* **2023**, *10*, 2201586.

(60) Peci, E.; Petrini, N.; Curreli, N.; Spotorno, E.; Tofighi, N. K.; Magnozzi, M.; Scotognella, F.; Kriegel, I.; Bisio, F. Fast thickness mapping of large-area exfoliated two-dimensional transition metal dichalcogenides by imaging spectroscopic ellipsometry. *EPJ. Web Conf* **2024**, *309*, 06006.

(61) Ramò, L.; Peci, E.; Magnozzi, M.; Spotorno, E.; Venturino, V.; Sygletou, M.; Giordano, M. C.; Zambito, G.; Telesio, F.; Milosz, Z.; et al. Noninvasive Deterministic Nanostructures Lithography on 2D Transition Metal Dichalcogenides. *Adv. Eng. Mater.* **2025**, *27*, 2401157.

(62) McCreary, K. M.; Hanbicki, A. T.; Sivaram, S. V.; Jonker, B. T. A- and B-exciton photoluminescence intensity ratio as a measure of sample quality for transition metal dichalcogenide monolayers. *APL Mater.* **2018**, *6*, 111106.

(63) Kriegel, I.; Ghini, M.; Bellani, S.; Zhang, K.; Jansons, A. W.; Crockett, B. M.; Koskela, K. M.; Barnard, E. S.; Penzo, E.; Hutchison, J. E.; et al. Light-Driven Permanent Charge Separation across a Hybrid Zero-Dimensional/Two-Dimensional Interface. *J. Phys. Chem. C* **2020**, *124*, 8000−8007.

(64) Christopher, J. W.; Goldberg, B. B.; Swan, A. K. Long tailed trions in monolayer MoS_2: Temperature dependent asymmetry and resulting red-shift of trion photoluminescence spectra. *Sci. rep.* **2017**, *7*, 14062.

(65) Golovynskyi, S.; Datsenko, O. I.; Dong, D.; Lin, Y.; Irfan, I.; Li, B.; Lin, D.; Qu, J. Trion Binding Energy Variation on Photoluminescence Excitation Energy and Power during Direct to Indirect Bandgap Crossover in Monolayer and Few-Layer MoS_2. *J. Phys. Chem. C* **2021**, *125*, 17806−17819.

(66) Lee, H. S.; Kim, M. S.; Kim, H.; Lee, Y. H. Identifying multiexcitons in MoS_2 monolayers at room temperature. *Phys. Rev. B* **2016**, *93*, 140409.

(67) Peng, Z.; Lo, T. W.; Lei, D. Plasmonic-hot-electron mediated room-temperature generation of charged biexciton in monolayer WS_2. *Phys. Rev. Mater.* **2023**, *7*, 054002.

(68) Wei, X.; Yu, Z.; Hu, F.; Cheng, Y.; Yu, L.; Wang, X.; Xiao, M.; Wang, J.; Wang, X.; Shi, Y. Mo-O bond doping and related-defect assisted enhancement of photoluminescence in monolayer MoS_2. *AIP Adv.* **2014**, *4*, 123004.

(69) Wang, K.; Paulus, B. Toward a comprehensive understanding of oxygen on MoS_2: from reaction to optical properties. *J. Phys. Chem. C* **2021**, *125*, 19544−19550.

(70) Klement, P.; Steinke, C.; Chatterjee, S.; Wehling, T. O.; Eickhoff, M. Effects of the Fermi level energy on the adsorption of O_2 to monolayer MoS_2. *2D Mater.* **2018**, *5*, 045025.

(71) Atkin, P.; Lau, D. W. M.; Zhang, Q.; Zheng, C.; Berean, K. J.; Field, M. R.; Ou, J. Z.; Cole, I. S.; Daeneke, T.; Kalantar-Zadeh, K. Laser Exposure Induced Alteration of WS_2 Monolayers in the Presence of Ambient Moisture. *2D Mater.* **2018**, *5*, 015013.

(72) Panasci, S. E.; Schilirò, E.; Greco, G.; Cannas, M.; Gelardi, F. M.; Agnello, S.; Roccaforte, F.; Giannazzo, F. Strain, Doping, and Electronic Transport of Large Area Monolayer MoS_2 Exfoliated on Gold and Transferred to an Insulating Substrate. *ACS Appl. Mater. Interfaces* **2021**, *13*, 31248−31259.

(73) Romaniuk, Y. A.; Golovynskyi, S.; Litvinchuk, A. P.; Dong, D.; Lin, Y.; Datsenko, O. I.; Bosi, M.; Seravalli, L.; Babichuk, I. S.; Yukhymchuk, V. O.; et al. Influence of anharmonicity and interlayer interaction on Raman spectra in mono- and few-layer MoS_2: A computational study. *Physica E* **2022**, *136*, 114999.

(74) Rodriguez, A.; Velický, M. c. v.; Řáhová, J.; Zólyomi, V.; Koltai, J.; Kalbáč, M.; Frank, O. Activation of Raman modes in monolayer transition metal dichalcogenides through strong interaction with gold. *Phys. Rev. B* **2022**, *105*, 195413.

(75) Lee, C.; Yan, H.; Brus, L. E.; Heinz, T. F.; Hone, J.; Ryu, S. Anomalous lattice vibrations of single-and few-layer MoS_2. *ACS Nano* **2010**, *4*, 2695−2700.

(76) Pan, Y.; Li, S.; Rahaman, M.; Milekhin, I.; Zahn, D. R. T. Signature of lattice dynamics in twisted 2D homo/hetero-bilayers. *2D Mater.* **2022**, *9*, 045018.

(77) Castellanos-Gomez, A.; Roldán, R.; Cappelluti, E.; Buscema, M.; Guinea, F.; van der Zant, H. S. J.; Steele, G. A. Local Strain Engineering in Atomically Thin MoS_2. *Nano Lett.* **2013**, *13*, 5361−5366.

(78) Chakraborty, B.; Bera, A.; Muthu, D.; Bhowmick, S.; Waghmare, U. V.; Sood, A. Symmetry-dependent phonon renormalization in monolayer MoS_2 transistor. *Phys. Rev. B* **2012**, *85*, 161403.

(79) Mao, N.; Chen, Y.; Liu, D.; Zhang, J.; Xie, L. Solvatochromic effect on the photoluminescence of MoS_2 monolayers. *Small* **2013**, *9*, 1312−1315.

(80) Wang, P.; Gao, B.; Liu, W. In situ doping effect in monolayer MoS_2 via laser irradiation. *Nano Express* **2024**, *5*, 015018.

(81) Rao, R.; Carozo, V.; Wang, Y.; Islam, A. E.; Perea-Lopez, N.; Fujisawa, K.; Crespi, V. H.; Terrones, M.; Maruyama, B. Dynamics of cleaning, passivating and doping monolayer MoS_2 by controlled laser irradiation. *2D Mater.* **2019**, *6*, 045031.

(82) Michail, A.; Delikoukos, N.; Parthenios, J.; Galiotis, C.; Papagelis, K. Optical detection of strain and doping inhomogeneities in single layer MoS_2. *Appl. Phys. Lett.* **2016**, *108*, 173102.

(83) Golovynskyi, S.; Datsenko, O. I.; Pérez-Jiménez, A. I.; Kuklin, A.; Chaigneau, M.; Golovynskyi, A.; Golovynska, I.; Bosi, M.; Seravalli, L. Exciton and Trion at the Perimeter and Grain Boundary of CVD-Grown Monolayer MoS_2: Strain Effects Influencing Application in Nano-Optoelectronics. *ACS Appl. Nano Mater.* **2024**, *7*, 15570−15582.

(84) Chae, W. H.; Cain, J. D.; Hanson, E. D.; Murthy, A. A.; Dravid, V. P. Substrate-induced strain and charge doping in CVD-grown monolayer MoS_2. *Appl. Phys. Lett.* **2017**, *111*, 143106.

(85) Rao, R.; Islam, A. E.; Singh, S.; Berry, R.; Kawakami, R. K.; Maruyama, B.; Katoch, J. Spectroscopic evaluation of charge-transfer doping and strain in graphene/MoS_2 heterostructures. *Phys. Rev. B* **2019**, *99*, 195401.

(86) Ferrera, M.; Rahaman, M.; Sanders, S.; Pan, Y.; Milekhin, I.; Gemming, S.; Alabastri, A.; Bisio, F.; Canepa, M.; Zahn, D. R. T. Controlling excitons in the quantum tunneling regime in a hybrid plasmonic/2D semiconductor interface. *Appl. Phys. Rev.* **2022**, *9*, 031401.

(87) Fan, X.; Zheng, W.; Liu, H.; Zhuang, X.; Fan, P.; Gong, Y.; Li, H.; Wu, X.; Jiang, Y.; Zhu, X.; et al. Nonlinear photoluminescence in monolayer WS_2: Parabolic emission and excitation fluence-dependent recombination dynamics. *Nanoscale* **2017**, *9*, 7235−7241.

(88) Kerfoot, J.; Legge, E. J.; Collins, A.; Chauhan, J.; Rossnagel, K.; Beton, P. H.; Mellor, C. J.; Pollard, A. J.; Rance, G. A.; George, M. W. Benchmarking TERS and TEPL probes: towards a reference sample for quantification of near-field enhancement factors in gap and non-gap modes. *Analyst* **2025**, *150*, 3077−3088.

(89) McIntyre, N.; Spevack, P.; Beamson, G.; Briggs, D. Effects of argon ion bombardment on basal plane and polycrystalline MoS_2. *Surf. Sci.* **1990**, *237*, L390−L397.

(90) Shuxian, Z.; Hall, W. K.; Ertl, G.; Knözinger, H. X-ray photoemission study of oxygen and nitric oxide adsorption on MoS_2. *J. Catal.* **1986**, *100*, 167−175.

(91) Durbin, T. D.; Lince, J. R.; Didziulis, S. V.; Shuh, D. K.; Yarmoff, J. A. Soft X-ray photoelectron spectroscopy study of the interaction of Cr with MoS_2 (0001). *Surf. Sci.* **1994**, *302*, 314−328.

(92) Kondekar, N. P.; Boebinger, M. G.; Woods, E. V.; McDowell, M. T. In situ XPS investigation of transformations at crystallographically oriented MoS_2 interfaces. *ACS Appl. Mater. Interfaces* **2017**, *9*, 32394−32404.

(93) Baker, M.; Gilmore, R.; Lenardi, C.; Gissler, W. XPS investigation of preferential sputtering of S from MoS_2 and determination of MoS_x stoichiometry from Mo and S peak positions. *Appl. Surf. Sci.* **1999**, *150*, 255−262.

(94) Choi, J.-G.; Thompson, L. XPS study of as-prepared and reduced molybdenum oxides. *Appl. Surf. Sci.* **1996**, *93*, 143−149.

(95) Benoist, L.; Gonbeau, D.; Pfister-Guillouzo, G.; Schmidt, E.; Meunier, G.; Levasseur, A. X-ray photoelectron spectroscopy characterization of amorphous molybdenum oxysulfide thin films. *Thin Solid Films* **1995**, *258*, 110−114.

(96) Colton, R. J.; Guzman, A. M.; Rabalais, J. W. Electrochromism in some thin-film transition-metal oxides characterized by x-ray electron spectroscopy. *J. Appl. Phys.* **1978**, *49*, 409−416.

(97) Leung, Y.; Wong, P.; Mitchell, K.; Smith, K. X-ray photoelectron spectroscopy studies of the reduction of MoO_3 thin films by NH_3. *Appl. Surf. Sci.* **1998**, *136*, 147−158.

(98) Galtayries, A.; Wisniewski, S.; Grimblot, J. Formation of thin oxide and sulphide films on polycrystalline molybdenum foils: characterization by XPS and surface potential variations. *J. Electron Spectrosc. Relat. Phenom.* **1997**, *87*, 31−44.

(99) National Institute of Standards and Technology. *NIST X-ray Photoelectron Spectroscopy Database*, Version 5.0. URL: https://srdata.nist.gov/xps/ (accessed July 1, 2025).

(100) Kondratenko, S.; Datsenko, O. I.; Golovynskyi, S.; Mykytiuk, A.; Kuklin, A.; Ågren, H.; Dzhagan, V.; Zahn, D. R. Deep level transient spectroscopy and theoretical modelling of defect states in few-layer MoS_2. *Surf. Interfaces* **2025**, *72*, 106928.

(101) Kim, J. Y.; Gelczuk, Ł.; Polak, M. P.; Hlushchenko, D.; Morgan, D.; Kudrawiec, R.; Szlufarska, I. Experimental and theoretical studies of native deep-level defects in transition metal dichalcogenides. *npj 2D Mater. Appl.* **2022**, *6*, 75.

(102) Gelczuk, Ł.; Kopaczek, J.; Scharoch, P.; Komorowska, K.; Blei, M.; Tongay, S.; Kudrawiec, R. Probing Defects in MoS_2 Van der Waals Crystal through Deep-Level Transient Spectroscopy. *Phys. Status Solidi RRL* **2020**, *14*, 2000381.

(103) Zhao, Y.; Tripathi, M.; Čerņevičs, K.; Avsar, A.; Ji, H. G.; Gonzalez Marin, J. F.; Cheon, C.-Y.; Wang, Z.; Yazyev, O. V.; Kis, A. Electrical spectroscopy of defect states and their hybridization in monolayer MoS_2. *Nat. Commun.* **2023**, *14*, 44.

(104) Mitterreiter, E.; Schuler, B.; Micevic, A.; Hernangómez-Pérez, D.; Barthelmi, K.; Cochrane, K. A.; Kiemle, J.; Sigger, F.; Klein, J.; Wong, E.; et al. The role of chalcogen vacancies for atomic defect emission in MoS_2. *Nat. Commun.* **2021**, *12*, 3822.